Laboratory investigations of iceberg capsize dynamics, energy dissipation and tsunamigenesis

J. C. Burton,[1] J. M. Amundson,[2] D. S. Abbot,[2] A. Boghosian,[2] L. M. Cathles,[2] S. Correa-Legisos,[3] K. N. Darnell,[2] N. Guttenberg,[1] D. M. Holland,[4] and D. R. MacAyeal[2]

Received 4 April 2011; revised 7 November 2011; accepted 11 November 2011; published 20 January 2012.

[1] We present laboratory experiments designed to quantify the stability and energy budget of buoyancy-driven iceberg capsize. Box-shaped icebergs were constructed out of low-density plastic, hydrostatically placed in an acrylic water tank containing freshwater of uniform density, and allowed (or forced, if necessary) to capsize. The maximum kinetic energy (translational plus rotational) of the icebergs was ~15% of the total energy released during capsize, and radiated surface wave energy was ~1% of the total energy released. The remaining energy was directly transferred into the water via hydrodynamic coupling, viscous drag, and turbulence. The dependence of iceberg capsize instability on iceberg aspect ratio implied by the tank experiments was found to closely agree with analytical predictions based on a simple, hydrostatic treatment of iceberg capsize. This analytical treatment, along with the high Reynolds numbers for the experiments (and considerably higher values for capsizing icebergs in nature), indicates that turbulence is an important mechanism of energy dissipation during iceberg capsize and can contribute a potentially important source of mixing in the stratified ocean proximal to marine ice margins.

Citation: Burton, J. C., J. M. Amundson, D. S. Abbot, A. Boghosian, L. M. Cathles, S. Correa-Legisos, K. N. Darnell, N. Guttenberg, D. M. Holland, and D. R. MacAyeal (2012), Laboratory investigations of iceberg capsize dynamics, energy dissipation and tsunamigenesis, *J. Geophys. Res.*, *117*, F01007, doi:10.1029/2011JF002055.

1. Introduction

[2] Iceberg capsize liberates a large amount of gravitational potential energy into the ocean over a relatively short period of time [*MacAyeal et al.*, 2011; *Levermann*, 2011]. This energy has multiple impacts, including (1) causing horizontal translation, vertical bobbing, and rocking of the iceberg and any adjacent sea ice and icebergs [*MacAyeal et al.*, 2003; *Amundson et al.*, 2010]; (2) generating a wide spectrum of ocean surface gravity waves, including meter-scale short period (<60 s) and several centimeter–scale long-period (100s of s) waves [*Amundson et al.*, 2008, 2010; *Nettles et al.*, 2008; *MacAyeal et al.*, 2009]; (3) stimulating calving or iceberg fragmentation through ice-ice contact or wave-driven ice shelf flexure [*MacAyeal et al.*, 2009]; (4) turbulently mixing stratified proglacial waters, thereby affecting ocean heat flux into and within a fjord (which depends on stratification [see *Motyka et al.*, 2003; *Straneo et al.*, 2010]); (5) generating unique seismic signals when the icebergs come into contact with the glacier terminus [*Tsai et al.*, 2008]; and (6) dissipating as heat into the water. In addition, the geometry and gravitational stability of an iceberg determines both its sensitivity to capsize and the total amount of potential energy released during capsize [*MacAyeal et al.*, 2011]. Iceberg geometry may therefore be an important parameter for the observed rapid (hours to days) disintegration of Antarctic ice shelves [*MacAyeal et al.*, 2003]. Moreover, the sizable tsunamic waves generated by iceberg capsize may contribute to the violent and rapid nature of these large-scale collapse events [*MacAyeal et al.*, 2011].

[3] In its simplest form, the energy budget of a capsizing iceberg can be expressed as

$$-\Delta U(t) = \Delta K_i(t) + \Delta E_w(t) + \Delta E_s(t) + \Delta E_m(t) + \Delta E_h(t), \quad (1)$$

where ΔU is the change in potential energy, K_i is the kinetic energy of the iceberg and any adjacent sea ice and icebergs (referred to as ice mélange), E_w and E_s are the energy of ocean waves and seismic waves, E_m is energy that is consumed by vertical mixing of the water column (dense parcels move upward), E_h is heat, and t is time. The expression is explicitly written as a function of time to allow for the fact that kinetic energy and wave energy ultimately ends up as heat. The relative importance of (and relationships between) the energy terms in equation (1) is unknown due to inherent dangers and difficulties of instrumenting remote, ice-choked

[1]Department of Physics, University of Chicago, Chicago, Illinois, USA.
[2]Department of Geophysical Sciences, University of Chicago, Chicago, Illinois, USA.
[3]Departamento de Física, Universidad de Santiago de Chile, Santiago, Chile.
[4]Courant Institute of Mathematical Sciences, New York University, New York, New York, USA.

0148-0227/12/2011JF002055

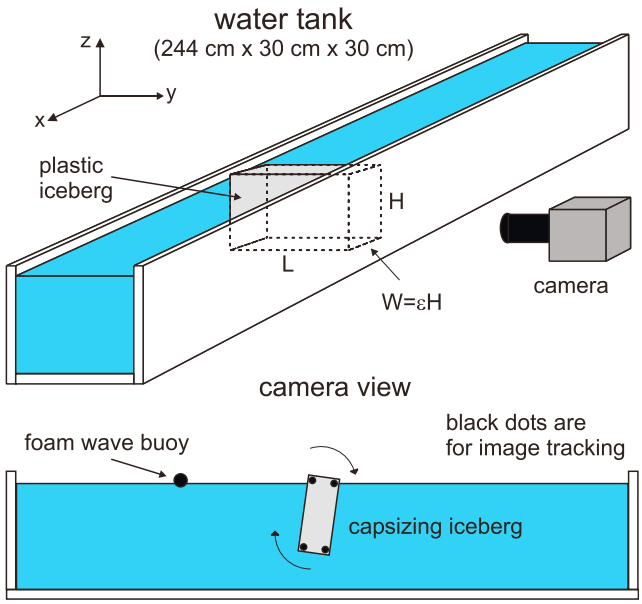

Figure 1. (top) Diagram of the laboratory setup. (bottom) The camera's field of view.

fjords. Such knowledge is desirable for two reasons. First, icebergs that capsize while calving into the ocean contain information (in the form of ocean and seismic waves) that can be used to investigate the processes controlling calving. Second, some processes that affect calving rates (ocean heat flux, ice mélange strength, and ice shelf flexure) may be influenced by the energy released during calving and its immediate aftereffects, i.e., iceberg capsize. It is worth noting some other forms of energy not considered in equation (1), such as elastic energy released by the fracturing of stressed ice, as well as the potential energy gained by the "rafting" of one piece of ice melange atop another. We assume these forms of energy are insignificant, and will ignore them in our analysis.

[4] As a first step toward quantifying the capsize energy budget, we present a laboratory investigation into the capsize dynamics of single icebergs starting from a state of rest that are in an 'open ocean' environment. Although many icebergs capsize in close proximity to the calving terminus and other icebergs, and may do so simultaneously with detachment from the sourceterminus, we began our laboratory investigation with the most simple and tractable end-member: the isolated iceberg in open water. The laboratory apparatus involved synthetic, box-shaped "icebergs" placed hydrostatically into a transparent aquarium tank containing fresh water. The icebergs were allowed (or forced, depending on their aspect ratio) to capsize; the icebergs' motion and coincident surface gravity waves were recorded with a digital video camera. In this study, our primary motivations were to (1) quantify iceberg stability conditions, (2) quantify the amount and rate of potential energy dissipation via viscous and turbulent motions in the water caused by capsize, and (3) place a bound on the maximum amplitude of and amount of energy contained in surface gravity waves generated by capsizing icebergs. Subsequent studies will consider iceberg capsize in stratified water bodies and iceberg-iceberg interactions during calving.

2. Experimental Methods

2.1. Laboratory Setting

[5] The laboratory model "fjord" consisted of an optically clear acrylic aquarium tank that is 244 cm long, 30 cm wide, and 30 cm tall (Figure 1), and has walls that are 1.3 cm thick. The tank was filled with fresh tap water at room temperature of density $\rho_w = 997$ kg m^{-3}. The depth of the water, D, was varied from 11.4 to 24.3 cm. The icebergs used in the experiments were machined out of low-density polyethylene plastic that had a density of $\rho_i = 920 \pm 1$ kg m^{-3}, which was calculated by measuring the mass and dimensions of the icebergs. For all icebergs the precapsize height, H, and length parallel to the axis of rotation during capsize, L, were held constant at 10.3 cm and 26.7 cm, respectively. The length L was chosen to be slightly shorter than the transverse width of the tank (30 cm) in order to minimize contact friction with the tank walls due to small rotations of the icebergs in the x-y plane. The width of the icebergs, W, was varied from 2.5–10.2 cm, so that the aspect ratio $\varepsilon = W/H$ varied from approximately 0.25 to 1.0.

[6] In order to measure the height of the waves produced by a capsizing iceberg, a small, spherical, closed cell styrofoam buoy was placed approximately 25 cm from the iceberg at the beginning of each run. This distance is sufficiently close to the capsize event so that waves reflected off the walls of the tank do not affect our wave amplitude measurements. Due to the very low density of the styrofoam, the buoy was well coupled to the water surface and thus measured the height of the water's surface at that location as a function of t. The experiments were recorded with a Casio EX-FH20 video camera, which was set to record 30 frames per second. The camera resolution was typically 16 pixels cm^{-1}, although we increased the resolution to 93 pixels cm^{-1} (by zooming in) to measure buoy displacements.

[7] In order to track the positions and angular orientations of the icebergs, black sticker dots were placed in each corner of the rectangular face of the icebergs (Figure 1). The position of each dot was located in each frame of the movie using custom feature-tracking software written in Mathematica (Wolfram Research). Once the positions of the dots were known in every movie frame, the center of mass of the iceberg was calculated as the mean position of the four dots, and the angular orientation was calculated by measuring the vector angle between the vertical (gravitational) direction and the direction of the iceberg parallel to the height H. All angles reported here are measured between the H axis and the vertical, which ranges from −90° to 90°. Although the camera was leveled before each video session, small tilts were still possible within our measurement accuracy. To provide a good measurement of the vertical direction in each video, we used the water level as a perpendicular plane to the vertical. The water level line was extracted from the first frame of each video, fitted to a linear model $z = (tan\ \theta_w)\ x + b$, and the resulting angle θ_w was subtracted from all other angles measured in the video.

2.2. Dynamic and Geometric Similarity

[8] As with any laboratory model of geological phenomena, a discussion of dynamic similitude is warranted [e.g., *Hubbert*, 1937; *Hughes*, 1993]. Our iceberg capsize experiments are defined by four dimensionless numbers. The first two are the aspect ratio, $\varepsilon = W/H$, and the density ratio, ρ_i/ρ_w, where ρ_i and ρ_w are the densities of the icebergs (plastic or ice) and the water. For more complicated iceberg geometries a single parameter such as the aspect ratio will not suffice. Many freshly calved icebergs are roughly box shaped (especially those involving full glacier thickness fracture [e.g., *Amundson et al.*, 2008; *Scambos et al.*, 2009; *Walter et al.*, 2010]), which gives support for the idealized geometries considered here. In the experiments the aspect ratio is varied so as to span a range of observed aspect ratios, and the density ratio differs from field observations by about 3%. We also only consider floating icebergs, so that capsize is not affected by the corners of the iceberg touching the ocean floor. In this regime the main role of water depth D will be to affect the speed of gravity waves in the water.

[9] For our modest-sized laboratory experiments, it is relevant to consider whether surface tension forces could be important for the iceberg dynamics. These effects can be addressed by inspection of the dispersion relation for surface waves in the presence of gravity and surface tension [*Lamb*, 1932]:

$$\omega^2 = \left(gk + \frac{\gamma}{\rho_w}k^3\right)\tanh(Dk), \tag{2}$$

where ω is the angular frequency, $k = 2\pi/\lambda$ is the wave number, λ is the wavelength, and γ is the surface tension. For a depth $D = 0.15$ m and a wavelength $\lambda = H \approx 0.1$ m, the period of the wave is ≈ 0.25 seconds. This differs by only $\sim$1% from the case where $\gamma = 0$. Thus, we conclude that for the wavelength and period of waves observed in our laboratory model, surface tension should be only a minor effect, and will be ignored in any further analysis.

[10] The other two dimensionless numbers defining the experiments are the Froude (Fr) and Reynolds (Re) numbers, which are the most important numbers for similitude in an overwhelming majority of coastal hydrodynamic phenomena [*Hughes*, 1993]. The Froude number describes how efficiently the iceberg can act as a source of gravitational waves and, is given by the ratio of the characteristic capsize velocity, V_{cap}, to the gravitational wave speed in water: $Fr = V_{cap}/V_{wave}$. The Reynolds number determines whether the fluid flow is turbulent or laminar and is given by a ratio of the inertial to viscous forces during capsize: $Re = (HV_{cap}\rho_w)/\mu$, where $\mu \approx 1.0$ mPa $\cdot$ s is the viscosity of water.

[11] We define V_{cap} by noting that the kinetic energy of a capsizing iceberg is limited by the total amount of potential energy released during capsize, E_{cap}. If we assume that this kinetic energy is in the form of translational motion only, then

$$V_{cap} = \sqrt{\frac{2E_{cap}}{m}}, \tag{3}$$

where $m = \rho_i \varepsilon H^2 L$ is the iceberg's mass. This is simply an upper bound on the translational velocity of the iceberg, and the actual characteristic translational velocities will be a fraction of V_{cap} due to energy dissipation into the water. (An alternative estimate of V_{cap} based on the kinetic energy of rotational motion is more complicated and yields a result that is comparable to the estimate associated with translational motion.) For the idealized iceberg geometries considered here, E_{cap} is given by

$$E_{cap} = \frac{1}{2}\rho_i g L H^3 \varepsilon(1-\varepsilon)\left(1 - \frac{\rho_i}{\rho_w}\right), \tag{4}$$

where g is gravitational acceleration [see *MacAyeal et al.*, 2011]. Inserting equation (4) into equation (3) yields

$$V_{cap} = \sqrt{\left(1 - \frac{\rho_i}{\rho_w}\right) gH(1-\varepsilon)}. \tag{5}$$

[12] To estimate the gravitational wave speed, V_{wave}, we take advantage of the dispersion relation for gravitational surface waves in the absence of surface tension and the definition of group velocity. The dispersion relation is given by setting $\gamma = 0$ in equation (2)

$$\omega^2 = gk\tanh(Dk), \tag{6}$$

We expect the wavelength of the generated waves to be of similar length to the iceberg height, so that $\lambda \approx H$. Furthermore, the water depth must exceed the initial iceberg height, such that $D = \beta H$ where $\beta \geq 1$. Inserting these relations into equation (6) gives

$$\omega^2 = gk\tanh(2\pi\beta) \approx gk. \tag{7}$$

Noting that the group velocity is given by $V_{wave} = \partial\omega/\partial k$, we find that

$$V_{wave} \approx \sqrt{\frac{gH}{8\pi}}. \tag{8}$$

Finally, inserting equations (5) and (8) into the expressions for the Froude and Reynolds numbers gives

$$Fr = \sqrt{8\pi\left(1 - \frac{\rho_i}{\rho_w}\right)(1-\varepsilon)}, \tag{9}$$

and

$$Re = F_r \frac{\rho_w}{\mu}\sqrt{\frac{gH^3}{8\pi}}. \tag{10}$$

[13] The Froude number is independent of iceberg height and is a simple function of 2 nondimensional numbers: the aspect ratio and the density ratio. As discussed above, the aspect ratios of the synthetic icebergs were varied to cover the range seen in field observations, whereas the density ratio differed from that associated with glacier ice by about 3%. The difference in the density ratio results in a Froude number that is $\sim$10% larger in the experiments than in the field. Additionally, equation (9) predicts that in both cases,

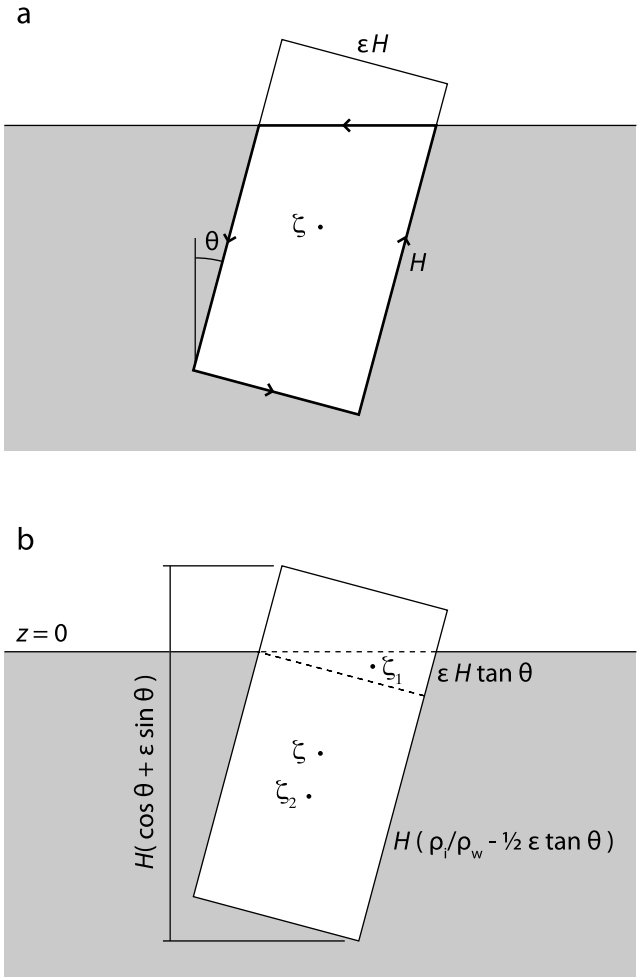

Figure 2. Schematic diagrams of iceberg cross sections. (a) Parameters needed for calculating an iceberg's gravitational potential energy. The contour used for the integral in equation (15) is indicated by the thick black line. (b) Parameters used to calculate the center of mass and center of buoyancy for an iceberg that is held in hydrostatic equilibrium (see section 3.1).

$Fr \approx 1$; however, we will later show that the above treatment overestimates the maximum kinetic energy, and therefore velocity, of the iceberg. The key point, however, is that $Fr < 1$ for both the experiments and the field, and this implies that radiation of energy as surface gravity waves will have a relatively minor contribution to the energy budget in both cases.

[14] The Reynolds number, on the other hand, depends on $H^{3/2}$. All other terms are roughly equivalent between the lab and the field. For an iceberg that is initially 100–1000 m thick, $Re = 10^8 - 10^{10}$. Such large Reynolds numbers indicate that iceberg capsize is a highly turbulent process. The Reynolds number of the experiments is $Re \approx 2 \times 10^4$ or 4–6 orders of magnitude smaller than in the field. Fortunately, the laboratory value for Re is sufficiently large that turbulence should be a dominant mechanism of energy dissipation, thus allowing us to compare our results to field observations and to provide a reasonable estimate of the capsizing iceberg energy budget. To be more specific, we note that turbulent drag forces on solid bodies have a quadratic dependence on velocity:

$$F_d = \frac{1}{2} C \rho_w A_c v^2, \tag{11}$$

where v is the velocity, A_c is the cross-sectional reference area, and C is the drag coefficient, which will depend on the geometry of the object and surface roughness. If we use V_{cap} as the velocity and H^2 as our area, we see that the drag force $F_d \propto H^3$, so that F_d scales with the mass of the iceberg, as does gravitational forces. For turbulent flow, drag coefficients typically vary by less than an order of magnitude even as the Reynolds number varies by many orders, so that the motion of a large iceberg ($H \approx 1$ km) may be well modeled in our laboratory experiments.

3. Iceberg Energetics

3.1. Gravitational Potential Energy

[15] The gravitational potential energy of an iceberg, U (equation (1)), can be expressed as the potential energy of the submerged portion of the iceberg in a reduced gravity environment plus the potential energy of the subaerial portion ofthe iceberg, such that

$$U = g(\rho_i - \rho_w) L \zeta_s A_s + g \rho_i L (A - A_s) \left(\frac{\zeta A - \zeta_s A_s}{A - A_s} \right), \tag{12}$$

where ζ is the elevation of the center of mass, ζ_s is the elevation of the center of buoyancy, and A and A_s are the cross-sectional areas of the iceberg and the submerged portion of the iceberg. All elevations are measured with respect to the waterline. Here we have assumed that $L > H$; thus the iceberg can only capsize in the x-z plane (as shown in Figures 1 and 2). The last two terms on the right hand side of equation (12) are equal to the area and center of mass of the subaerial portion of the iceberg. Rearranging equation (12) and noting that $A = \varepsilon H^2$ for our idealized icebergs gives

$$U = g \rho_i L \varepsilon H^2 \zeta - g \rho_w L \zeta_s A_s. \tag{13}$$

The center of buoyancy, after applying Green's theorem, is given by

$$\zeta_s = -\frac{1}{2A_s} \oint_c z_s^2 dx, \tag{14}$$

where z_s is the vertical position of a submerged boundary element of the iceberg and c indicates that a contour integral is performed around that boundary. Inserting equation (14) into equation (13), we find that

$$U = g \rho_i L \varepsilon H^2 \zeta + \frac{1}{2} g \rho_w L \oint_c z_s^2 dx. \tag{15}$$

[16] In this formulation, $U = 0$ if the iceberg disintegrates into infinitesimally small pieces that float on the water surface. The contour integral in equation (15) can be determined explicitly for rectangular icebergs having arbitrary orientation, θ, and elevation, ζ. However, the analytic

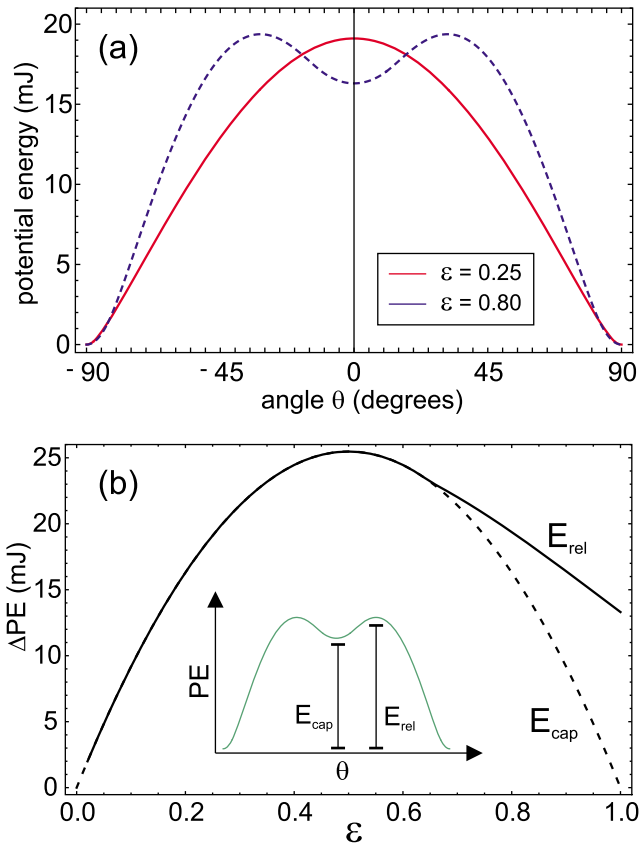

Figure 3. (a) Calculated gravitational potential energy of a plastic iceberg as it is hydrostatically rotated through 90°. The red curve ($\varepsilon = 0.25$) is unstable to small perturbations from an initial orientation of $\theta = 0$. For $\varepsilon = 0.8$, the iceberg cannot spontaneously capsize from its initial orientation because small rotations increase the potential energy. (b) Potential energy difference from capsize (E_{cap}, equation (4)) and actual energy release (E_{rel}) in our experiments. For $\varepsilon > \varepsilon_c$, the iceberg must be rotated over an energy barrier before it will capsize, so the energy released E_{rel} is greater than E_{cap}.

solution is lengthy and piecewise; we therefore choose to calculate it numerically. We also note that equation (15) yields the same total energy release during capsize, E_{cap} (equation (4)), as was found by *MacAyeal et al.* [2011].

3.2. Iceberg Capsize Stability Analysis

[17] One ramification of equation (15) is that rectangular icebergs with aspect ratios larger than some critical value, ε_c, will not capsize unless an energy barrier is overcome by some external agent. Furthermore, by investigating the potential energy curves of icebergs with various aspect ratios (Figure 3a), it becomes evident that $\varepsilon_c < 1$. In other words, an iceberg can be narrower than it is tall yet still not be capable of spontaneously capsizing.

[18] The value of ε_c can be determined by placing an iceberg in hydrostatic equilibrium and investigating the change in torque on the iceberg, which is given by $\tau = -\partial U/\partial\theta$, as the iceberg is rotated away from vertical. For small angular rotations ($\theta \ll 1°$) the center of rotation is assumed to lie on the waterline ($z = 0$), and thus the submerged area of the iceberg is

$$A_s = \varepsilon H^2 \frac{\rho_i}{\rho_w}. \tag{16}$$

This assumption allows us to simplify equation (13) to

$$U = g\rho_i L\varepsilon H^2(\zeta - \zeta_s). \tag{17}$$

Thus the torque on an iceberg due to buoyancy is given by

$$\tau = g\rho_i L\varepsilon H^2 \frac{\partial}{\partial\theta}(\zeta_s - \zeta). \tag{18}$$

Due to the idealized geometry used here, ζ and ζ_s can be determined explicitly (for small θ) through investigation of Figure 2. Since the iceberg is held in hydrostatic equilibrium we require that

$$A_s = (\rho_i/\rho_w)\varepsilon H^2. \tag{19}$$

Equation (19) allows us to determine the lengths of the submerged portion of the iceberg (Figure 2b), from which it follows that the vertical elevation of the iceberg's center of mass is

$$\zeta = -H\cos\theta\left(\frac{\rho_i}{\rho_w} - \frac{1}{2}\right). \tag{20}$$

We use geometric decomposition to calculate the center of buoyancy, such that

$$\zeta_s = \frac{\zeta_1 A_1 + \zeta_2 A_2}{A_s}, \tag{21}$$

where ζ_1 and A_1 are the center of mass and area of the small triangle in Figure 2b, and ζ_2 and A_2 are the center of mass and area of the rectangle located immediately below the triangle. The area and center of mass of the triangle are given by

$$A_1 = \frac{1}{2}(\varepsilon H)^2\tan\theta, \tag{22}$$

and

$$\zeta_1 = -\frac{1}{3}\varepsilon H\sin\theta. \tag{23}$$

The area and center of mass of the rectangle are given by

$$A_2 = \varepsilon H^2\left(\frac{\rho_i}{\rho_w} - \frac{1}{2}\varepsilon\tan\theta\right), \tag{24}$$

and

$$\zeta_2 = -\frac{H}{2}\cos\theta\left(\frac{\rho_i}{\rho_w} + \frac{1}{2}\varepsilon\tan\theta\right). \tag{25}$$

Inserting equations (19) and (22)–(25) into equation (21) gives

$$\zeta_s = -\frac{1}{2}\frac{\rho_w}{\rho_i}H\left[\frac{\varepsilon^2}{12}\sec\theta + \left(\left(\frac{\rho_i}{\rho_w}\right)^2 - \frac{\varepsilon^2}{12}\right)\cos\theta\right]. \tag{26}$$

Setting equation (18) equal to zero, inserting the equations for ζ and ζ_s (equations (20) and (26)), solving for ε, and letting $\theta \rightarrow 0$ gives

$$\varepsilon_c = \sqrt{6\frac{\rho_i}{\rho_w}\left(1-\frac{\rho_i}{\rho_w}\right)}, \tag{27}$$

which is in agreement with the expression derived by *MacAyeal et al.* [2003]. For icebergs in seawater, $\varepsilon_c \approx 0.75$, and for the plastic blocks and fresh water used in our experiments, $\varepsilon_c \approx 0.66$. For $\varepsilon > \varepsilon_c$, icebergs must be rotated to a sufficient angle so that they will capsize. We define E_{rel} as the amount of energy actually released in the capsize (Figure 3b). When $\varepsilon < \varepsilon_c$, then $E_{rel} = E_{cap}$ and the icebergs will spontaneously capsize at $\theta = 0$.

[19] From equation (18) it is clear that the torque exerted on an iceberg depends on the iceberg's aspect ratio. For small rotations from vertical, the torque achieves a maximum value at $\varepsilon = \varepsilon_o$ [see *Amundson et al.*, 2010, Figure 9], which can be evaluated analytically by setting $\partial\tau/\partial\varepsilon = 0$, solving for ε, and letting $\theta \rightarrow 0$. This gives

$$\varepsilon_o = \frac{\varepsilon_c}{\sqrt{3}}. \tag{28}$$

Icebergs with $\varepsilon = \varepsilon_o$ can exert the largest forces on adjacent ice blocks, at least during the initial phases of capsize, and thus may play an important role in initiating large-scale calving events by causing extension of a proglacial ice mélange or highly fractured ice shelf. (Note that the analytic solutions for ε_c and ε_o presented here are in perfect agreement with the values numerically calculated by *Amundson et al.* [2010].)

3.3. Oscillation Frequencies

[20] The equilibrium hydrostatic position of a rectangular iceberg of height H and width εH is

$$\begin{aligned} z_{eq} &= H\left(\frac{1}{2}-\frac{\rho_i}{\rho_w}\right) \\ \theta_{eq} &= 0. \end{aligned} \tag{29}$$

By comparing observed oscillations around this equilibrium with oscillation frequencies predicted from hydrostatic assumptions, we can assess the impact that hydrodynamic forces have on the dynamics of iceberg capsize. The oscillation frequencies can be predicted from Newton's equations of motion [see also *Schwerdtfeger*, 1980] for the 3 degrees of freedom (θ, x, and z):

$$\begin{aligned} I\ddot{\theta} &= -\frac{\partial U}{\partial \theta} + \nu_\theta |\dot{\theta}|^n \mathrm{sign}(\dot{\theta}) \\ m\ddot{x} &= -\frac{\partial U}{\partial x} + \nu_x |\dot{x}|^n \mathrm{sign}(\dot{z}) \\ m\ddot{z} &= -\frac{\partial U}{\partial z} + \nu_z |\dot{z}|^n \mathrm{sign}(\dot{z}), \end{aligned} \tag{30}$$

where $I = \rho_i \varepsilon (1+\varepsilon^2) H^4 L/12$ is the iceberg's moment of inertia around its center of mass, ν_θ, ν_x, and ν_z are simple damping coefficients that represent energy dissipation due to drag, and n determines whether energy is dissipated viscously ($n = 1$) or turbulently ($n = 2$). Since the potential energy does not depend on x (equation (15)), then $\partial U/\partial x = 0$ and the second of equations (30) can be ignored. Bobbing and rocking frequencies are associated with motion in the z and θ directions, respectively. Assuming a hydrostatic, frictionless fluid ($\nu_\theta = \nu_x = \nu_z = 0$) and small rocking oscillations (so that we can again use equation (17)), we find that

$$\begin{aligned} f_{bob} &= \frac{1}{2\pi}\sqrt{\frac{g\rho_w}{\varepsilon\rho_i}} \\ f_{rock} &= \frac{1}{2\pi}\sqrt{\frac{g\left(6\rho_i^2 - 6\rho_i\rho_w + \varepsilon^2\rho_w^2\right)}{H(1+\varepsilon^2)\rho_i\rho_w}}. \end{aligned} \tag{31}$$

[21] The bobbing frequency agrees with the analysis of *Schwerdtfeger* [1980]. However, *Schwerdtfeger* [1980] incorrectly calculated the rocking frequency because the analysis did not allow the iceberg's center of mass to change elevation during rocking. This is a reasonable simplification for very wide icebergs ($\varepsilon > 10$), but greatly overpredicts the natural rocking frequency of narrower icebergs. As an example, for a stable iceberg with $\varepsilon = 0.75$, *Schwerdtfeger* [1980] predicts a rocking frequency 118% higher than our value. Thus, icebergs that are barely stable are much more sensitive to lower-frequency ocean swell than was previously thought. Also, as expected, equation (31) indicates that the rocking period equals zero when $\varepsilon = \varepsilon_c$, and is imaginary when $\varepsilon < \varepsilon_c$ so that small perturbations will grow (leading to capsize) instead of oscillate.

4. Experimental Results

4.1. Iceberg Stability

[22] We performed a series of iceberg stability experiments to verify our derivation of iceberg potential energy (equation (15)). The synthetic icebergs were hydrostatically positioned with the height of the iceberg, H (see Figure 2), oriented vertically. The icebergs were then allowed (or forced) to capsize. The results are summarized in Figure 4. All icebergs with small aspect ratios ($\varepsilon < \varepsilon_c$) spontaneously capsized; the potential energy curves of these icebergs resemble the red curve ($\varepsilon = 0.5$) in Figure 3. Icebergs having aspect ratios close to ε_c have peculiar potential energy curves with shallow minima at $\theta \leq 15°$; these icebergs are unstable at $\theta = 0$ but are able to rest at some other finite angle (see the icebergs just to the right of the dashed line in Figure 4a). This peculiarity is a consequence of the rectangular geometry assumed here (e.g., the minimum disappears for rectangular icebergs with sufficiently rounded corners). Thus we leave it as a demonstration of the subtle relationship between iceberg geometry and stability. Finally, for larger values of ε, the icebergs had to be rotated (by slowly pulling on the icebergs with a thin piece of fishing wire) over a finite energy barrier before they would capsize (see the blue curve, for which $\varepsilon = 0.8$, in Figure 3). The results from stability experiments are in excellent agreement with our analytical derivations of iceberg stability, and thus support the derivation of iceberg potential energy presented above.

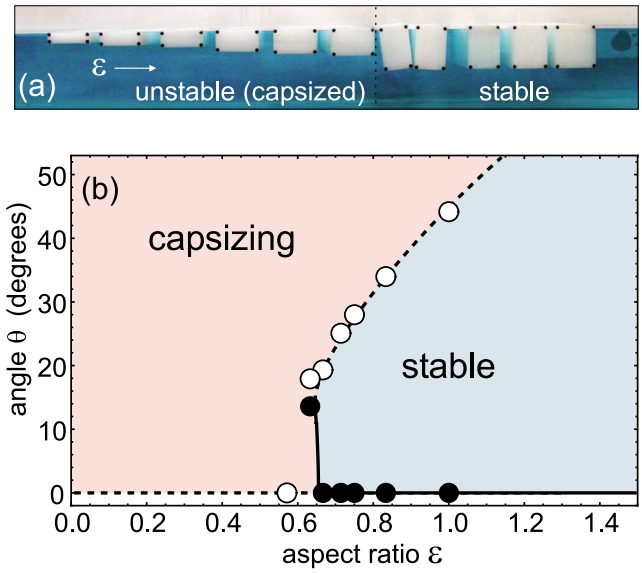

Figure 4. Results from iceberg stability analysis. (a) All plastic icebergs used in the experiment placed in order of increasing ε. When $\varepsilon < \varepsilon_c$, the icebergs are unstable and will spontaneously capsize. In the small area around ε_c they are stable at a finite angle, and at larger values they are stable in the upright ($\theta = 0$) orientation. (b) Stability diagram of box-shaped icebergs used in the experiments. For $\theta = 0$, the stable and unstable phases are separated by the critical aspect ratio, ε_c, given in equation (27). The dotted lines show unstable potential energy maximums, and the solid lines show stable potential energy minimums. The solid and open data points are measurements of stable angles (potential energy minima) and unstable equilibria (potential energy maxima).

4.2. Iceberg Dynamics and Kinetic Energy

[23] Some of the potential energy released during iceberg capsize is converted into translational and rotational kinetic energy of the iceberg, which we can directly track in the laboratory through image feature tracking. Typical measurements of the orientation, θ, and horizontal and vertical positions of the center of mass (ξ and ζ, respectively) are shown in Figure 5. As the iceberg rotates, θ goes from zero to 90° (the postcapsize equilibrium position). Iceberg capsize is followed by a short period of vertical and rotational oscillations. The oscillations are rapidly damped due to energy leaving the iceberg through wave generation and viscous and turbulent dissipation.

[24] The kinetic energies associated with iceberg rotation, KE_R, and horizontal and vertical translation, KE_X and KE_Z, are plotted in Figure 6a. The iceberg's kinetic energy is dominated by rotational energy, which peaks shortly before the iceberg has rotated 90°. The most striking result from these experiments is that only a small fraction of potential energy released during iceberg capsize is converted into iceberg kinetic energy (Figure 6b). The maximum kinetic energy of the iceberg is ~15% of the energy it released during capsize, and thus ~85% of the energy must be immediately released into the water (i.e., during the initial rotation of the iceberg from $\theta = 0°$ to $\theta = 90°$).

[25] The maximum power put into the water, $P_{\max}$, computed by taking the derivative of the total iceberg energy ($PE + KE_R + KE_Z + KE_X$) with respect to time, was found to depend on ε (Figure 7a). The general shape of the curve is likely due in large part to the total energy released during capsize, E_{cap}, which depends quadratically on ε and reaches a maximum at $\varepsilon = 0.5$ [*MacAyeal et al.*, 2011] (see equation (4)). Moreover, the power put into the water does not appear to depend on water depth within our experimental error. Note that the results from the stable region ($\varepsilon > \varepsilon_c$) are not as easily interpreted since the icebergs had to be slowly rotated to overcome a potential energy barrier prior to capsizing (see section 4.1). In Figure 7b, we show $P_{\max}$ in a dimensionless fashion scaled by the actual energy released E_{rel} (see Figure 3b), and a timescale $T_{rel} = H\sqrt{m/E_{rel}}$. When plotted in this way, a linear trend emerges which shows that larger icebergs produce more power per unit potential energy released.

[26] To explain this result, we note that a simple drag force on a capsizing iceberg (equation (30)) should be of the form $F_{drag} \propto \rho_i HL\dot{\theta}^n$, where the product $H \times L$ is the cross-

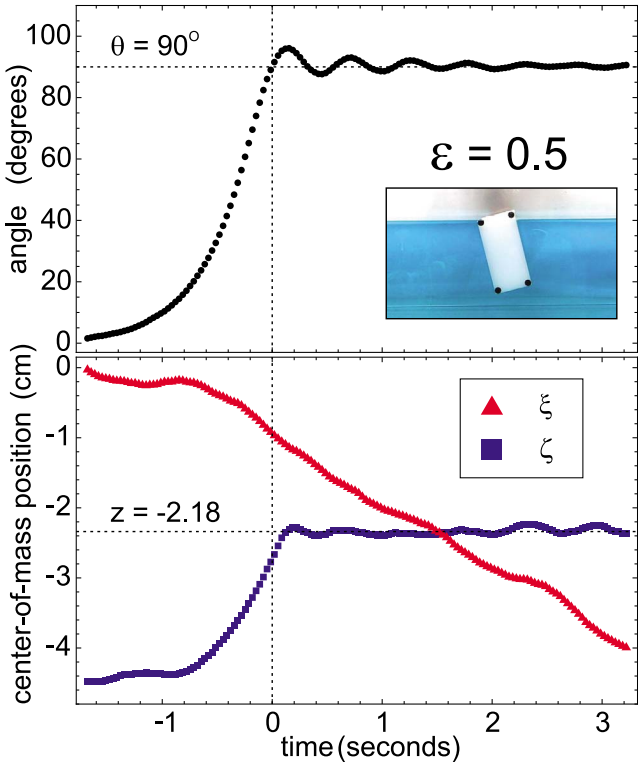

Figure 5. Rotation angle (θ) and center of mass in the x direction (ξ) and z direction (ζ) of an $\varepsilon = 0.5$ capsizing plastic iceberg. All data are shown with $t = 0$ corresponding to the time that the iceberg first rotated to $\theta = 90°$. The horizontal dotted lines indicate the capsized equilibrium angle and vertical position. During the capsize process, ζ increases because this lowers the iceberg's potential energy. The position of ξ changes more slowly, indicating that after capsize the iceberg translates due to momentum transfer to the water. In this example the iceberg translates to the left, indicating that there has been a transfer of momentum to the water in the form of waves traveling to the right.

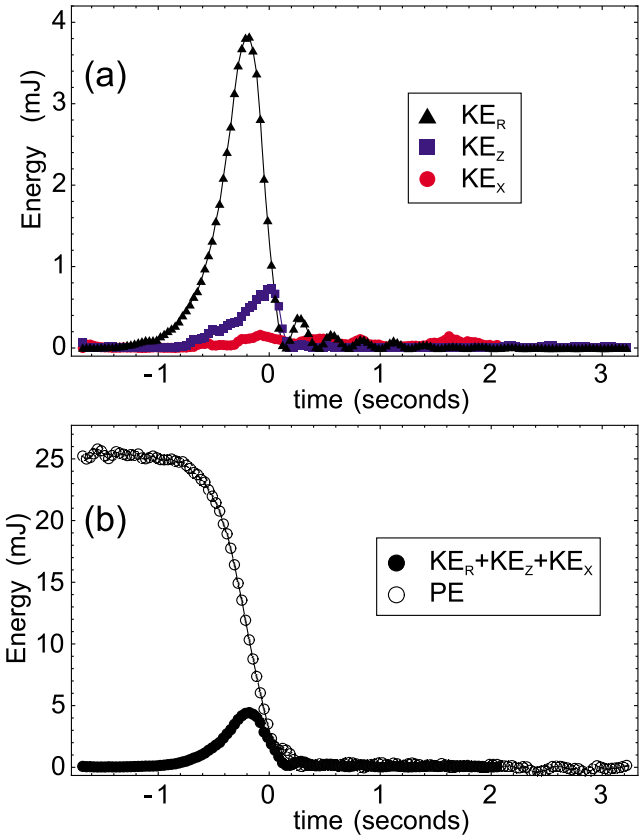

Figure 6. Measured energy of an $\varepsilon = 0.5$ iceberg during capsize. (a) Kinetic energies versus time. As the iceberg rotates and the center of mass moves upward, the rotational (KE_R) and z translational (KE_Z) energy increases. The x translational energy is quite small but can be a larger component of the total kinetic energy for icebergs with smaller ε. The rotational kinetic energy is clearly dominant. (b) Total kinetic energy and potential energy versus time. The maximum kinetic energy is roughly 15% of the total potential energy released.

sectional area sweeping out the water as the iceberg rotates. The gravitational capsizing force is proportional to the mass $m = \rho_i \varepsilon H^2 L$, so for icebergs with larger values of ε (and thus larger mass), the drag force has less of an effect on the dynamics. This fact can also be deduced from Figure 7c, which shows the maximum kinetic energy (rotational plus translational) scaled by E_{rel}. We see that for icebergs with larger ε, the maximum kinetic energy is a larger percentage of the total available potential energy.

[27] The large amount of energy put into the water is further illustrated by the horizontal motion of the icebergs during and following capsize (Figure 7d). If the icebergs did not transfer momentum to the water, their horizontal positions would remain fixed during capsize. Instead, we find that the icebergs tend to accelerate horizontally in the direction determined by the initial tilt of the upper surface. Thus an iceberg that rotates clockwise will move to the right. Icebergs with small values of ε translate horizontally the fastest, indicating that they transfer momentum to the water most efficiently.

4.3. Tsunami Energy and Amplitude

[28] Discriminating between the 2 mechanisms of energy delivered to the water (wave generation and dissipation) is not as straightforward as calculating iceberg potential and kinetic energies. We can estimate the surface wave energy, however, by measuring wave amplitudes with a buoy and assuming that the wavelength is approximately equal to the iceberg's height, H. Thus, the surface wave energy is given by

$$E_w = \frac{1}{8}\rho_w g A_w \Delta z^2, \tag{32}$$

where A_w is the map view area of a surface wave (wavelength times the width of the tank) and Δz is the crest-to-trough amplitude [*Gill*, 1982].

[29] We have made direct optical measurements of tsunami wave amplitudes by tracking the vertical displacements of a styrofoam buoy (Figure 8). The wave amplitude is a function of ε and, as expected, closely follows the maximum power input into the water (see Figure 7a) with the largest values occurring when $\varepsilon \approx 0.5$. Moreover, our results are in excellent agreement with the theoretical prediction that the maximum amplitude of glaciogenic tsunamis is $\approx 0.01H$ [*MacAyeal et al.*, 2011]; for our synthetic icebergs, this corresponds to an amplitude of 1 mm.

[30] From equation (32), we estimate that the energy of a capsize-generated wave with an amplitude of 2 mm is roughly 0.3 mJ. This accounts for a very small percentage of the total energy released during capsize (E_{cap}; equation (4)), which is 25 mJ for our synthetic icebergs when $\varepsilon = 0.5$. Thus, we conclude that the majority of iceberg potential energy is quickly dissipated during capsize, and may therefore be a source for considerable turbulent dissipation and mixing.

5. Validation of Simplified Iceberg Capsize Models and Implications for Ice Shelf Collapse

[31] Our laboratory experiments allow us to test whether iceberg capsize can be adequately characterized without accounting for hydrodynamics (i.e., the transfer of momentum from the iceberg to the water). This approximation can greatly reduce the complexity of ice shelf collapse models, which are inherently computationally expensive due to the thousands of iceberg collisions that must be modeled [*Guttenberg et al.*, 2011]. To test the hydrostatic capsize approximation, we fit modeled iceberg capsize trajectories (using equation (30)). The initial orientation and elevation of the icebergs were specified from data, and ν_θ and ν_z were adjusted to minimize the error between the data and model results. In this simplified model the force balance in the x direction is 0 and therefore the second of equation (30) is ignored. The start time of the minimization was taken as the point at which the iceberg had rotated to $\theta = 10°$; the end time was 3 s later. This was done to avoid fitting oscillations associated with (1) initial placement of the iceberg and (2) waves reflecting off of the walls of the tank.

[32] The simplest choice of a drag force law would be using $n = 1$ in equation (30). However, as Figure 9 illustrates, we have strong evidence for significant turbulent flow in the water during the capsize of our laboratory icebergs.

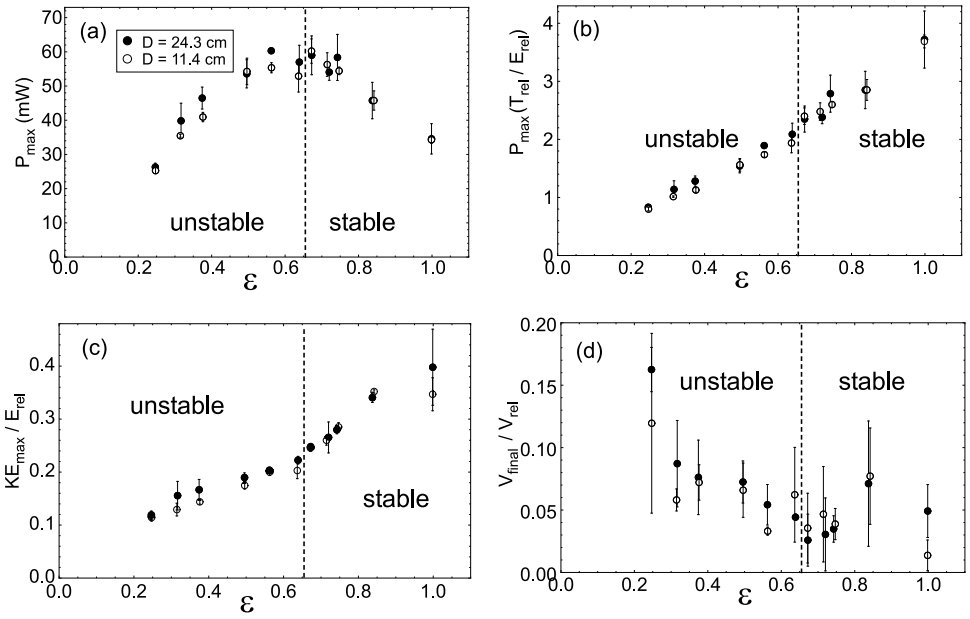

Figure 7. Observations of energy transfer to the water. Open and solid circles represent data taken at two different water depths, D. The error bars represent the standard deviation of three different capsize events. The boundary between the stable and unstable regimes is $\varepsilon = \varepsilon_c$. (a) Maximum power put into the water ($P_{\max}$) during capsize as a function of ε. (b) $P_{\max}$ scaled by E_{rel} and T_{rel}, as defined in the text. Icebergs with a larger ε achieve a relatively higher rate of energy dissipation. (c) Maximum kinetic energy of the icebergs versus ε. $KE_{\max}$ is able to reach higher percentages of the total available energy as ε is increased. (d) Final translational velocity of the icebergs in the x direction after capsize. Icebergs with smaller values of ε have a more asymmetric capsize process, resulting in better momentum transfer to the water and subsequent horizontal iceberg motion.

Thus the minimization was done for both $n = 1$ (laminar viscous dissipation) and $n = 2$ (turbulent dissipation). The results of the minimization, which are shown in Figure 10, have multiple implications. First, the model fits the data quite well for both $n = 1$ and $n = 2$, although the misfit is about 10% lower for the latter. This suggests that turbulence is an important energy sink, as is expected from the estimated Reynolds number (see section 2.2). Turbulence should be even more important in the field, where capsizing icebergs have Reynolds numbers that are orders of magnitude larger.

[33] Second, an important source of error in the minimizations is that the frequency of iceberg oscillations in the model is larger than observed. When $\varepsilon = 0.5$ the modeled frequencies are ~5% too large, whereas when $\varepsilon = 0.25$ the frequencies are ~30% too large. We attribute these discrepancies to the fact that the model does not transfer momentum to the water, which is supported by the observation that icebergs with small values of ε tend to translate horizontally during capsize (see section 4.2). Future simplified iceberg capsize models may require the use of "added mass effects" to account for this momentum transfer [*Brennen*, 1982].

[34] Finally, the rate at which icebergs capsize and expand out into the ocean during an ice shelf collapse event depends, in part, on the rate of energy dissipation into the ocean due to viscous drag (or turbulence) [*Guttenberg et al.*, 2011]. The values of ν_z and ν_θ found here (Figures 10c and 10d) are likely lower than encountered in the field, where dissipation is expected to be highly turbulent. The Guttenberg model assumes that ice shelf collapse is not rate limited by fracture propagation (i.e., prior to collapse the ice shelf has already disaggregated into uncapsized icebergs). Thus, when the laboratory-derived values of ν_z and ν_θ are applied to the Guttenberg model, we find that a maximum of 20% of the icebergs in a fully disaggregated, large ice shelf (producing 100 s of icebergs) can capsize during the first 8 h of a collapse event.

6. Possible Impacts of Energy Dissipation on Fjord Properties

[35] Possibly the most important finding of this study is that the majority of the energy released by a capsizing iceberg is rapidly dissipated into the water as the iceberg rotates from $\theta = 0°$ to $\theta = 90°$. Furthermore, much of the dissipation is likely due to turbulence. In many cases, iceberg capsize is the result of a calving event when the newly formed iceberg is gravitationally unstable. Here we use our results to quantitatively assess the impact of calving events on fjord stratification. Iceberg calving and capsize has implications for fjord dynamics and stratification because (1) turbulence does work against stratification and therefore affects heat transport in fjords, which depends on stratification [see, e.g., *Motyka et al.*, 2003; *Straneo et al.*, 2010; *Mortensen et al.*, 2011] and (2) hydrodynamic dissipation increases the heat content of the proglacial water, possibly influencing submarine melt rates or sea ice growth.

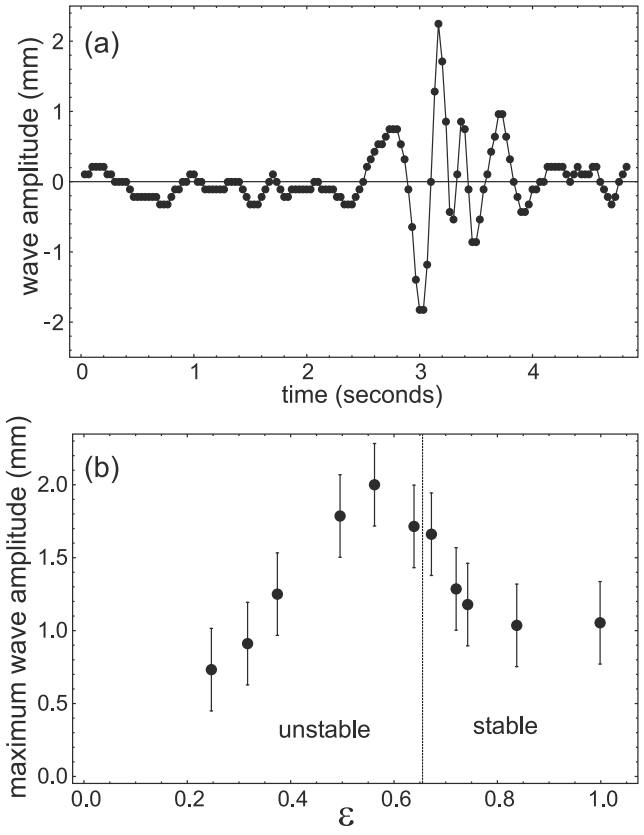

Figure 8. Measured amplitudes of waves generated by capsizing, plastic icebergs. In all cases, the styrofoam wave buoy was placed about 25 cm (a distance of 2.5*H*) away from the iceberg's center of mass. (a) Wave amplitude versus time for an $\varepsilon = 0.56$ iceberg. The iceberg capsized at $t \approx 1.5$ s. The small fluctuations in amplitude prior to and after the event are associated with experimental noise and disturbances associated with placement of the iceberg in the tank. The tsunami begins with a small crest that is followed by a large trough; the main wave crest arrives shortly afterward. (b) Maximum wave amplitude versus ε. Error bars represent the small fluctuations in the water surface prior to the wave arrival. Each point is the average of three measurements.

[36] Field observations of calving-generated turbulence are completely lacking, and thus we are unable to fully quantify the impacts of calving-generated mixing and heat generation on fjord dynamics and temperature. Moreover, our laboratory model presently consists of freshwater of uniform temperature, and so any energy lost to turbulence will ultimately be converted to heat. We can, however, provide a first assessment of these processes by using an example from Jakobshavn Isbræ, Greenland (Figure 11a) to consider the two end-members: all of the dissipated energy is (1) consumed by vertical, adiabatic mixing of the water column, or (2) converted into heat in the vicinity of the glacier terminus. Icebergs at Jakobshavn Isbræ are typically 1000 m tall, 500 m wide (perpendicular to axis of rotation), and 1000 m wide (parallel to axis of rotation) (Figure 11b). Throughout much of the summer, these icebergs are released from a glacier terminus that is at or close to floatation. When these icebergs capsize, the energy released is about 10^{14} J

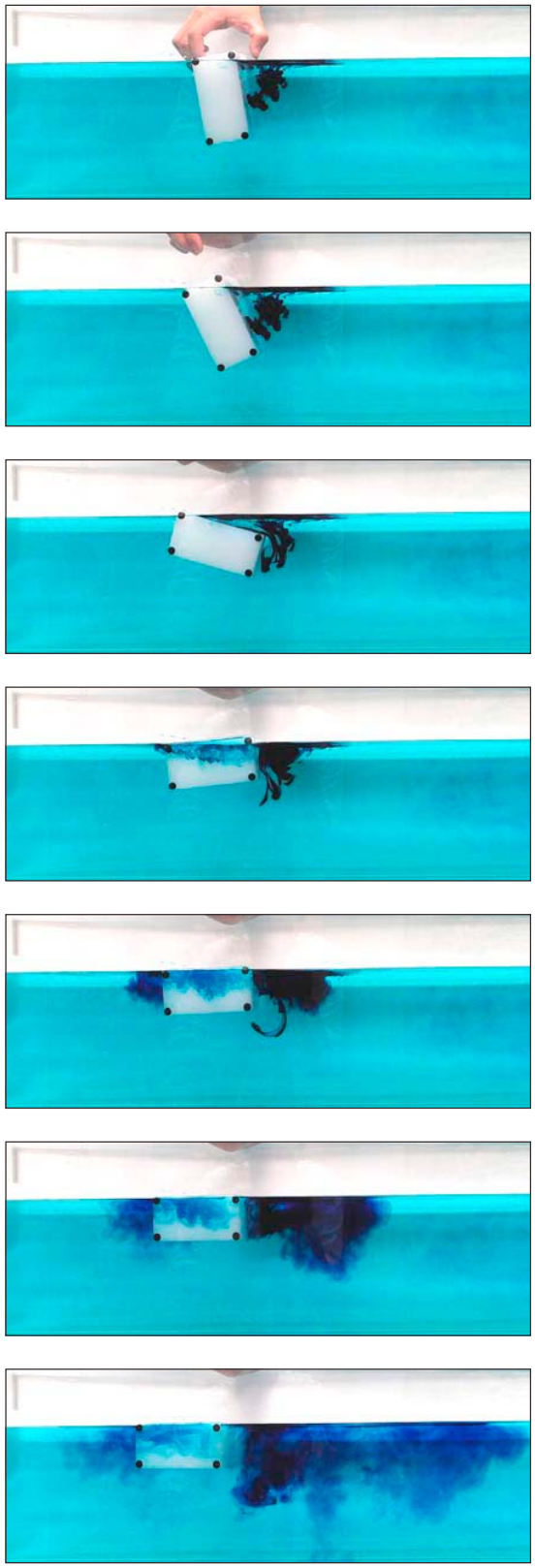

Figure 9. Video frames showing the capsize of an $\varepsilon = 0.5$ plastic iceberg. The dark blue dye to the right of the berg shows the pattern of flow and the development of a large vortex indicative of turbulent flow. The dye and thus the mixing flow extends far away from the right side of the iceberg. The time between the first and last frame is 12 s.

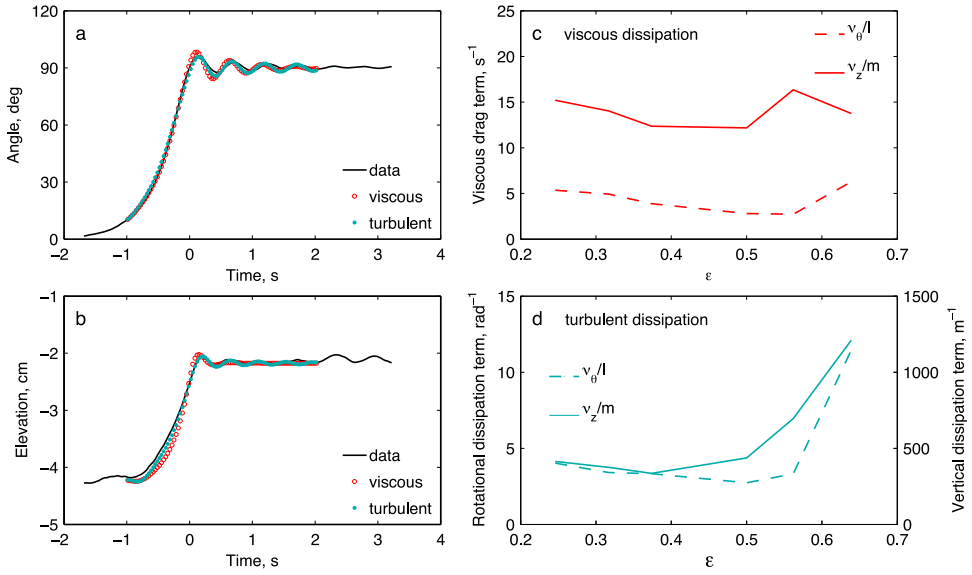

Figure 10. Results from fitting a hydrostatic iceberg capsize model to experimental data. (a) Iceberg orientation from vertical and (b) elevation of the iceberg's center of mass for an iceberg with $\varepsilon = 0.5$. Black curves represent experimental data, and red and green curves are the best fit solutions for laminar viscous ($n = 1$) and turbulent ($n = 2$) dissipation, respectively. (c) Best fit viscous drag terms for various iceberg aspect ratios. (d) Best fit turbulent drag terms for various iceberg aspect ratios.

(see equation (4)). Roughly 30 calving events of this size occur each year [*Amundson et al.*, 2008, 2010].

6.1. Case I: All of the Dissipated Energy Is Consumed in Adiabatic Mixing

[37] Turbulent mixing changes the gravitational potential energy of a water column by changing the column's vertical density profile. The change in potential energy of a column per unit surface area due to mixing is

$$E_m = \int_0^{H_w} (\tilde{\rho}_w(z) - \rho_w(z))gzdz, \tag{33}$$

where H_w is the total water depth, ρ_w and $\tilde{\rho}_w$ are water density prior to and after mixing, and z is the upward pointing vertical coordinate.

[38] Complete mixing of a column through adiabatic processes produces a column with constant salinity, potential density, and potential temperature. Using (1) data from XCTD casts made in the fjord in July 2008 (Figures 11a and 11c–11e), which are assumed to be representative of the entire fjord; (2) the equation of state of seawater [e.g., *Gill*, 1982]; (3) conservation of mass, salt, and thermal energy; and (4) the requirement that the mixed column has constant salinity, potential density, and potential temperature, we estimate that the energy needed to achieve complete adiabatic mixing of the water column is 9×10^5 J m^{-2}. Although this estimate is based on just a few profiles collected during a short time interval, it does provide an order of magnitude estimate of the energy needed for mixing.

[39] The energy dissipated during a single calving event, if it went entirely into mixing, would be sufficient to mix about 100 km^2 of the fjord (by surface area). Only 5% of the energy would be needed to entirely mix the innermost 1 km of fjord (which is 5 km wide at the glacier terminus). Such localized mixing may still be important because, proximal to the terminus, it could impact the upwelling and outflow of subglacial discharge [see *Motyka et al.*, 2003; *Rignot et al.*, 2010; *Straneo et al.*, 2011], and further down fjord, it could modify the strength and structure of circulation including outflow at subsurface levels [e.g., *Mortensen et al.*, 2011]. Since observations of fjord conditions immediately adjacent to a glacier terminus are lacking, we would only be able to speculate on how calving-generated mixing might affect fjord circulation.

[40] Observations from Sermilik Fjord [*Straneo et al.*, 2011] provide some, albeit ambiguous, indication that calving-generated turbulence is an important process in tidewater glacier fjords. Their (limited) observations indicate that Sermilik Fjord is most strongly stratified in winter, when calving events are rare, and most weakly stratified in summer, when calving events occur frequently. We thus hypothesize that calving events strongly influence fjord stratification on seasonal timescales.

6.2. Case II: All of the Dissipated Energy Is Converted Into Heat

[41] As a result of turbulent mixing in the water column, energy released by a capsizing iceberg will increase the heat content of a fjord. If all of the energy released by a capsizing iceberg is converted into heat, then the temperature of some volume of water, V_w, will increase by

$$\Delta T = \frac{E_{cap}}{\rho_w V_w C_p}, \tag{34}$$

where $C_p \approx 4000$ Jkg^{-1} °C^{-1} is the specific heat capacity [*Gill*, 1982] and ΔT is the change in water temperature. From equation (34), we find that a typical calving iceberg at Jakobshavn Isbræ can, for example, increase the temperature

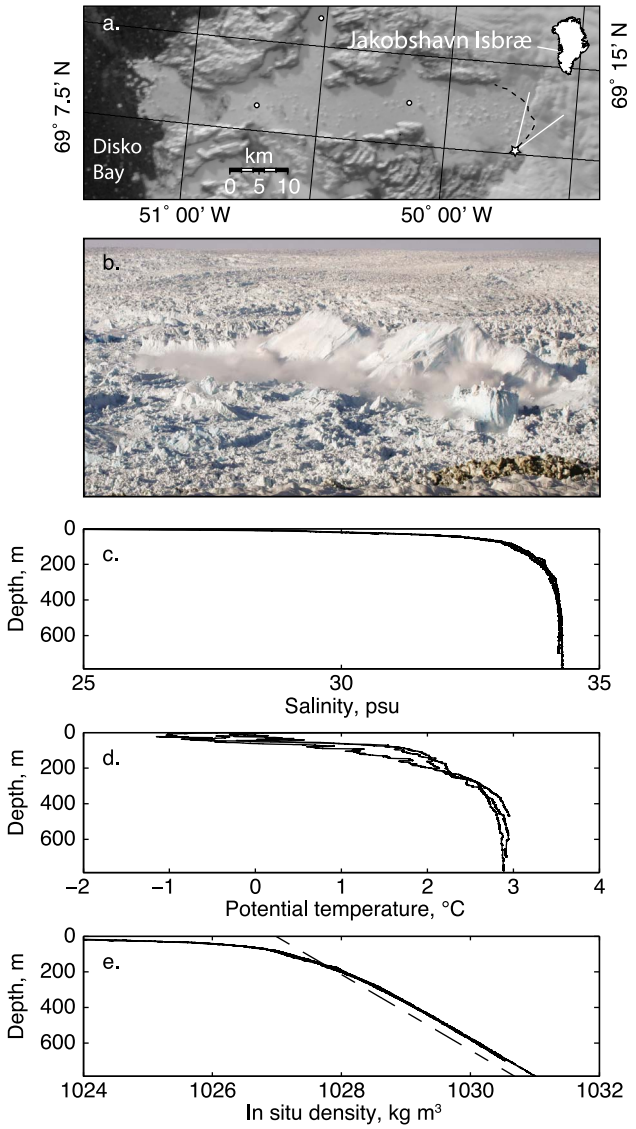

Figure 11. (a) MODIS image of Jakobshavn Isbræ indicating the terminus position, the position of XCTD casts made in the fjord on 29 and 30 July 2008, and (b) the position and look angle of the camera used to take the photo. Figure 11b shows a typical calving iceberg, captured on 10 May 2008. (c–e) Salinity, potential temperature, and in situ density profiles collected in the fjord. The dashed curve in Figure 11e is the density profile that indicates perfect adiabatic mixing of the water column (i.e., constant salinity, potential temperature, and potential density).

of 2.5 km^3 of water by 0.01°C. We suspect that such small changes in water temperature will have little impact on fjord dynamics.

[42] Heat generated by capsizing icebergs may also act as a source for melting of sea ice, icebergs, and a glacier's terminus. Assuming that the ice being melted is already at its melting point, the volume of ice that can be melted, V_i, with the heat generated by a single capsizing iceberg is

$$V_i = \frac{E_{cap}}{\rho_i l_f}, \tag{35}$$

where $l_f = 3.34 \times 10^5$ Jkg^{-1} is the latent heat of fusion for ice [*Paterson*, 1994]. Thus, individual icebergs that calve from Jakobshavn Isbræ can produce, at most, enough heat to melt 0.01 km^3 of ice. The ice flux through the glacier's terminus region (which is melted or calved into the ocean) is approximately 46 km^3 yr^{-1} [*Rignot and Kanagaratnam*, 2006]. Taking this as an upper bound for the calving flux, we estimate that the heat generated by calving can currently melt up to 0.92 km^3 of ice in a year. This source of heat is small but not entirely insignificant. As an order of magnitude comparison, we note that *Motyka et al.* [2011] estimated that prior to its recent calving retreat the floating tongue of Jakobshavn Isbræ was experiencing submarine melt rates on the order of 21 km^3 yr^{-1}.

7. Conclusions

[43] The energy released by calving and capsizing icebergs has implications for fjord stratification and dynamics, ice shelf collapse and ice mélange dynamics, and generation of ocean and seismic waves. The laboratory-scale study presented here indicates that (1) the maximum kinetic energy of a capsizing iceberg is about 15% of the total energy released by the iceberg, (2) about 1% of the energy is radiated away from the iceberg as ocean surface gravity waves, (3) calving-generated ocean waves should have a maximum amplitude that is approximately equal to 1% of the iceberg's initial thickness (as was predicted by *MacAyeal et al.* [2011]), and, perhaps most importantly, (4) the majority of the liberated energy is rapidly dissipated into the ocean through viscous drag and/or turbulence.

[44] The amount of mixing that is caused by calving events remains uncertain but is a unique and potentially important process within fjords containing tidewater glaciers. By disrupting fjord stratification, calving events may affect heat transport and melting within a fjord. This heat transport, in turn, can affect a glacier's stability by melting submarine portions of the terminus [*Motyka et al.*, 2003] and/or by influencing the strength of a coverage of sea ice or ice mélange [*Reeh et al.*, 2001; *Amundson et al.*, 2010]. Further work involving field, laboratory, and modeling studies is needed in order to determine both the amount of mixing caused by calving icebergs and the amount of time it takes a fjord to recover from a single calving event or a seasonally modulated series of calving events.

[45] **Acknowledgments.** Funding for this project was provided by the U.S. National Science Foundation (ANT0944193, ANT0732869, ANS0806393, and DMR-0807012). D.S.A. was supported by the T. C. Chamberlin Fellowship of the University of Chicago and the Canadian Institute for Advanced Research. We thank the Fultz family for supporting the hydrodynamics laboratory at the University of Chicago. Comments from A. Jenkins, M. Funk, an anonymous reviewer, and editor M. Truffer greatly improved the clarity of this manuscript.

References

Amundson, J. M., M. Truffer, M. P. Lüthi, M. Fahnestock, M. West, and R. J. Motyka (2008), Glacier, fjord, and seismic response to recent large calving events, Jakobshavn Isbræ, Greenland, *Geophys. Res. Lett.*, *35*, L22501, doi:10.1029/2008GL035281.

Amundson, J. M., M. Fahnestock, M. Truffer, J. Brown, M. P. Lüthi, and R. J. Motyka (2010), Ice mélange dynamics and implications for terminus stability, Jakobshavn Isbræ, Greenland, *J. Geophys. Res.*, *115*, F01005, doi:10.1029/2009JF001405.

Brennen, C. E. (1982), A review of added mass and fluid inertial forces, *Tech. Rep. CR82.010*, Nav. Civ. Eng. Lab., Dep. of the Navy, Port Hueneme, Calif.

Gill, A. E. (1982), *Atmosphere-Ocean Dynamics*, 662 pp., Academic, San Diego, Calif.

Guttenberg, N., D. S. Abbot, J. M. Amundson, J. C. Burton, L. M. Cathles, D. R. MacAyeal, and W. W. Zhang (2011), A computational investigation of iceberg capsize as a driver of explosive ice-shelf disintegration, *Ann. Glaciol.*, *52*(59), 51–59.

Hubbert, M. K. (1937), Theory of scale models as applied to the study of geologic structures, *Geol. Soc. Am. Bull.*, *48*(10), 1459–1519.

Hughes, S. A. (1993), *Physical Models and Laboratory Techniques in Coastal Engineering*, 550 pp., World Sci., River Edge, N. J.

Lamb, H. (1932), *Hydrodynamics*, 6th ed., 738 pp., Cambridge Univ. Press, Cambridge, U. K.

Levermann, A. (2011), Oceanography: When glacial giants roll over, *Nature*, *472*, 43–44, doi:10.1038/472043a.

MacAyeal, D. R., T. A. Scambos, C. L. Hulbe, and M. A. Fahnestock (2003), Catastrophic ice-shelf break-up by an ice-shelf-fragment-capsize mechanism, *J. Glaciol.*, *49*(164), 22–36.

MacAyeal, D. R., E. A. Okal, R. C. Aster, and J. N. Bassis (2009), Seismic observations of glaciogenic ocean waves (micro-tsunamis) on icebergs and ice shelves, *J. Glaciol.*, *55*(190), 193–206.

MacAyeal, D. R., D. S. Abbot, and O. V. Sergienko (2011), Iceberg-capsize tsunamigenesis, *Ann. Glaciol.*, *52*(58), 51–56.

Mortensen, J., K. Lennert, J. Bendtsen, and S. Rysgaard (2011), Heat sources for glacial melt in a subarctic fjord (Godthåbsfjord) in contact with the Greenland Ice Sheet, *J. Geophys. Res.*, *116*, C01013, doi:10.1029/2010JC006528.

Motyka, R. J., L. Hunter, K. A. Echelmeyer, and C. Connor (2003), Submarine melting at the terminus of a temperate tidewater glacier, LeConte Glacier, Alaska, U.S.A., *Ann. Glaciol.*, *36*, 57–65.

Motyka, R. J., M. Fahnestock, M. Truffer, J. Mortensen, and S. Rysgaard (2011), Submarine melting of the 1985 Jakobshavn Isbræ floating tongue and the triggering of the current retreat, *J. Geophys. Res.*, *116*, F01007, doi:10.1029/2009JF001632.

Nettles, M., et al. (2008), Step-wise changes in glacier flow speed coincide with calving and glacial earthquakes at Helheim Glacier, Greenland, *Geophys. Res. Lett.*, *35*, L24503, doi:10.1029/2008GL036127.

Paterson, W. S. B. (1994), *The Physics of Glaciers*, 3rd ed., 481 pp., Butterworth-Heinemann, Oxford, U. K.

Reeh, N., H. H. Thomsen, A. K. Higgins, and A. Weidick (2001), Sea ice and the stability of north and northeast Greenland floating glaciers, *Ann. Glaciol.*, *33*, 474–480.

Rignot, E., and P. Kanagaratnam (2006), Changes in the velocity structure of the Greenland Ice Sheet, *Science*, *311*, 986–990, doi:10.1126/science.1121381.

Rignot, E., M. Koppes, and I. Velicogna (2010), Rapid submarine melting of the calving faces of West Greenland glaciers, *Nat. Geosci.*, *3*, 187–191, doi:10.1038/ngeo765.

Scambos, T., H. A. Fricker, C.-C. Liu, J. Bohlander, J. Fastook, A. Sargent, R. Massom, and A.-M. Wu (2009), Ice shelf disintegration by plate bending and hydro-fracture: Satellite observations and model results of the 2008 Wilkins ice shelf break-ups, *Earth Planet. Sci. Lett.*, *280*, 51–60.

Schwerdtfeger, P. (1980), Iceberg oscillations and ocean waves, *Ann. Glaciol.*, *1*, 63–65.

Straneo, F., G. S. Hamilton, D. A. Sutherland, L. A. Stearns, F. Davidson, M. O. Hammill, G. B. Stenson, and A. Rosing-Asvid (2010), Rapid circulation of warm subtropical waters in a major glacial fjord in East Greenland, *Nat. Geosci.*, *3*, 182–186, doi:10.1038/ngeo764.

Straneo, F., R. G. Curry, D. A. Sutherland, G. S. Hamilton, C. Cenedese, K. Våge, and L. A. Stearns (2011), Impact of fjord dynamics and glacial runoff on the circulation near Helheim Glacier, *Nat. Geosci.*, *4*, 322–327, doi:10.1038/ngeo1109.

Tsai, V. C., J. R. Rice, and M. Fahnestock (2008), Possible mechanisms for glacial earthquakes, *J. Geophys. Res.*, *113*, F03014, doi:10.1029/2007JF000944.

Walter, F., S. O'Neel, D. McNamara, W. T. Pfeffer, J. N. Bassis, and H. A. Fricker (2010), Iceberg calving during transition from grounded to floating ice: Columbia Glacier, Alaska, *Geophys. Res. Lett.*, *37*, L15501, doi:10.1029/2010GL043201.

D. S. Abbot, J. M. Amundson, A. Boghosian, L. M. Cathles, K. N. Darnell, and D. R. MacAyeal, Department of the Geophysical Sciences, University of Chicago, 5734 S. Ellis Ave., Chicago, IL 60637, USA.

J. C. Burton and N. Guttenberg, Department of Physics, University of Chicago, 5720 S. Ellis Ave., Chicago, IL 60637, USA. (jcburton@uchicago.edu)

S. Correa-Legisos, Departamento de Física, Universidad de Santiago de Chile, Ave. Ecuador 3493, Estacion Central, Santiago 9170124, Chile.

D. M. Holland, Courant Institute of Mathematical Sciences, New York University, 251 Mercer St., New York, NY 10012, USA.